

Article

The Influence of the Precursor's Nature and Drying Conditions on the Structure, Morphology, and Thermal Properties of TiO₂ Aerogels

Jolanta Donėlienė^{1,2,*}, Eglė Fataraitė-Urbonienė^{1,3}, Nina Danchova⁴, Stoyan Gutzov⁴ and Juras Ulbikas^{1,2}

¹ Applied Research Institute for Prospective Technologies, Vismaliuku Str. 34, LT 10243 Vilnius, Lithuania; egle.fataraitė@ktu.lt (E.F.-U.); ulbikas@met.lt (J.U.)

² JSC Modern E-Technologies, Vismaliuku Str. 34, LT 10243 Vilnius, Lithuania

³ Faculty of Mechanical Engineering and Design, Kaunas University of Technology, Studentu Str. 56, LT 51424 Kaunas, Lithuania

⁴ Department of Physical Chemistry, Faculty of Chemistry and Pharmacy, Sofia University "St. Kliment Ohridski", J. Bourchier Blvd. 1, 1164 Sofia, Bulgaria; fhndd@chem.uni-sofia.bg (N.D.); sgutzov@chem.uni-sofia.bg (S.G.)

* Correspondence: jolanta.doneliene@met.lt; Tel.: +370-5250-0616

Abstract: A cost-effective solution for the synthesis of high-porosity TiO₂ aerogels, which can be used as a mesoporous perovskite network charge-carrier material during the manufacture of solar cells, is described. The effects of the synthesis parameters (precursor (titanium (IV) isopropoxide (TIP) and tetrabutyl orthotitanate (TBOT)), additional solvent exchange (n-hexane (nH), cyclohexane (CH), and diethyl ether (DE)), subcritical drying (800 mbar vacuum, 70 °C, 8 h), aging, and calcination on the aerogel's structure have been investigated. Methods of XRD, FT-IR, BET, Raman, STA, SEM, UV-vis, and thermal conductivity measurements were applied to find out the relation between the synthesis conditions and the properties of the synthesized aerogels. Amorphous aerogels are polydispersed systems with the highest probability of pore diameter from 0.5 to 15 nm. An nH-exchanged, aged aerogel synthesized from the precursor TIP shows the highest diameter of pores. After calcination, the aerogels tend to crystallize into an anatase phase and the size of the crystallites depends on the precursor's nature. Calcination leads to a significant increase in both the apparent and true density of the aerogels, and it also results in an increase in porosity and thermal conductivity.

Keywords: TiO₂ aerogel; sol-gel synthesis; solvent exchange; ageing; subcritical drying; thermal conductivity



Citation: Donėlienė, J.; Fataraitė-Urbonienė, E.; Danchova, N.; Gutzov, S.; Ulbikas, J. The Influence of the Precursor's Nature and Drying Conditions on the Structure, Morphology, and Thermal Properties of TiO₂ Aerogels. *Gels* **2022**, *8*, 422. <https://doi.org/10.3390/gels8070422>

Academic Editor: Saad Khan

Received: 8 June 2022

Accepted: 4 July 2022

Published: 6 July 2022

Publisher's Note: MDPI stays neutral with regard to jurisdictional claims in published maps and institutional affiliations.



Copyright: © 2022 by the authors. Licensee MDPI, Basel, Switzerland. This article is an open access article distributed under the terms and conditions of the Creative Commons Attribution (CC BY) license (<https://creativecommons.org/licenses/by/4.0/>).

1. Introduction

Aerogels are three-dimensional solid materials with the following characteristics: pore sizes ranging from 2 to 50 nm, a very high open porosity, and a specific surface area [1]. Aerogels have some variations, such as organic aerogels (cellulose [2], etc.), carbon aerogels [3] (usually carbonized from organic aerogels), and oxide aerogels (silica [4], alumina [5], zirconia [6], and titania [7]). Titanium dioxide (TiO₂) is considered one of the most well-known photocatalysts due to its efficient photocatalytic activities [8], low cost, and safety for human health [9] and the environment [10]. Titania can also be used in other applications, such as photocatalytic water splitting, removal of pollutants from the environment [11,12], solar cells [13], rechargeable batteries [14], sensors, supercapacitors, and biomedical devices [13,15]. In particular, for solar cell applications, a mesoporous TiO₂ with a large specific surface area is essential to increase the amount of dye adsorption [16,17] or perovskite adsorption, as well as the power conversion efficiency [18,19].

Titania can be synthesized using different methods, such as dry methods (flame synthesis and chemical vapor deposition), wet chemistry methods (the chloride (TiCl₄) method and hydrothermal processing) [12], and sol-gel methods [20]. Moreover, different

techniques can be used for wet gels obtained by sol–gel method drying, which include the following: supercritical drying [7,20,21], freeze drying [22], post-pyrolysis, ambient drying [23], and subcritical drying [24].

The synthesis routes of the mesoporous TiO₂ oxide involve many process parameters that can determine the mesoporous structure (i.e., Ti-alkoxide concentration, pH, surrounding media, aging time [25], solvents, etc.) [26]. Gel aging can increase cross-linking and can result in the creation of aerogels with excellent pore sizes, as well as large surface areas [27]. For the additional solvent exchange, different solvents with low surface tensions can be used, which can lower the surface tension of the pore liquid of the hydrogel. Surface tension can be decreased by applying a solvent exchange and, therefore, preventing capillary pressure from damaging the aerogel network during the drying process [28].

Understanding the mechanism of the synthesis route and determining the optimal synthesis parameters allows for selecting the most cost-effective set of aerogel synthesis conditions at which the required structural and morphological properties are obtained. In previous work [29], it was found that subcritical dried samples (400 mbar, 70 °C, 8 h) show an amorphous structure, which after calcination tends to crystallize in the anatase phase and affect the microstructure of the aerogels. The originally obtained aerogels show structural and optical properties comparable to TiO₂ structures mentioned in the literature and appear to be quite promising for photovoltaic applications.

This investigation focuses on cost-effective solutions for the synthesis of high-porosity TiO₂ aerogels, which can be used as mesoporous perovskite network charge-carrier materials for solar cell production. The next step and goal of the investigation was to evaluate the influence of lowering down the vacuum to 800 mbar on the properties of TiO₂ aerogels. The influence of the precursor type, gel aging, additional solvent exchange, and other synthesis parameters that control the formation of the TiO₂ aerogels has also been investigated.

2. Results and Discussion

To understand the effects of the synthesis conditions on the structural characteristics of TiO₂ aerogels, different analysis methods, such as X-ray diffraction (XRD), Fourier-transform infrared spectroscopy (FT-IR), Brunauer–Emmett–Teller (BET), Raman spectroscopy, simultaneous thermal analysis (STA), scanning electron microscopy (SEM), ultraviolet–visible (UV–vis) spectroscopy, and thermal conductivity measurements, were applied to identify and discuss trends for further aerogel structural optimizations.

2.1. XRD Analysis

Figure S1 shows XRD patterns that characterize the structure of synthesized subcritical dried (800 mbar, 70 °C, 8 h) TiO₂ aerogels in relation to the nature of the precursor (titanium (IV) isopropoxide (TIP) and tetrabutyl orthotitanate (TBOT)), the type of solvent used for the additional exchange (n-hexane (nH), cyclohexane (CH), diethyl ether (DE)), and the effects of ageing (72 h, 40 °C). All investigated TiO₂ aerogel samples show an amorphous structure [30] (Figure S1).

2.2. FT-IR Analysis

The FT-IR spectra of the TiO₂ aerogels are presented in Figure 1. When comparing the obtained curves, it can be stated that significant differences between them do not occur. The characteristic peaks between 400 and 1000 cm^{−1} can be attributed to the bending vibration of the Ti–O–Ti and the stretching vibration of the Ti–O bonds [1,8,31]. These broad peaks in the mentioned range could also be attributed to a combination of Ti–O–Ti and Ti–O–C bond stretching vibrations [11].

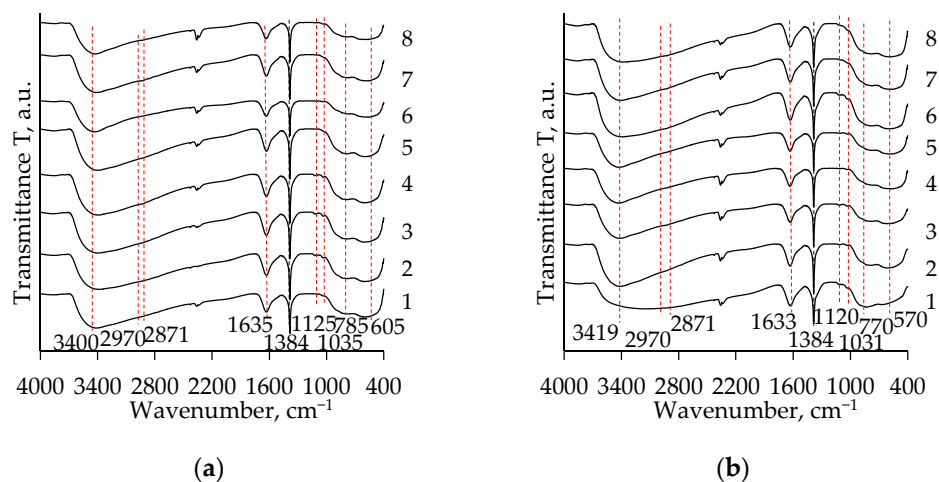


Figure 1. FT-IR spectra of the TiO_2 aerogels after subcritical drying (800 mbar, 70°C , 8 h) without aging (1–4) and after 72 h of aging (5–8) depending on the precursor type (TIP (a), TBOT (b)) and the solvent used for an additional solvent exchange (1, 5—without exchange; 2, 6—CH; 3, 7—nH; 4, 8—DE).

The weak absorption peaks at $1040\text{--}1120\text{ cm}^{-1}$ can be attributed to the stretching vibration of the C–C bonds [21,31]. The peak at 1380 cm^{-1} is due to the symmetric deformation vibration of CH_3 [21]. The peaks at 2970 and 2871 cm^{-1} can be assigned, respectively, to symmetric CH_2 and CH_3 stretching [31]. Typically, these peaks characterize the remaining organic compounds (in this case, they can be dissociative organic solvents (nH, CH, and DE) and EtOH) in the pores of the TiO_2 aerogels [8,31]. The wide absorption bands at $\sim 1633\text{ cm}^{-1}$ and $\sim 3390\text{ cm}^{-1}$ can be related to the bending vibrations of the adsorbed water molecules (H–O–H) and the stretching vibrations of the hydroxyl (OH) groups on the surface of the aerogel, respectively [1,8,31].

2.3. BET Analysis

Figures 2–5 show the results of BET analysis of unaged and aged subcritical dried (800 mbar, 70°C , 8 h) TiO_2 aerogels synthesized using the precursor TBOT or TIP together with an additional solvent exchange in CH, nH, or DE. In all cases, the aerogels are polydisperse systems, the characteristics of which depend on the synthesis conditions, the precursor nature, and the type of solvent used for the additional exchange.

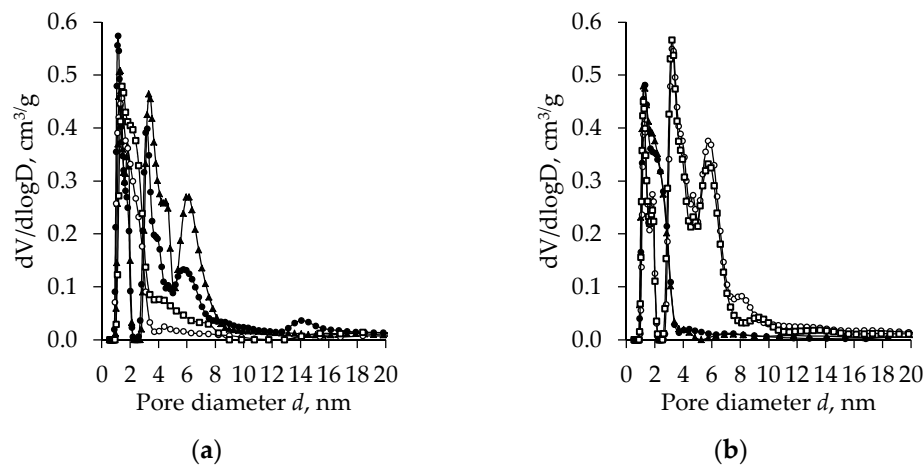


Figure 2. The pore size distribution of subcritical dried (800 mbar, 70°C , 8 h) TiO_2 aerogels synthesized using the TBOT precursor versus the type of exchange solvent (●—without exchange, ○—nH, ▲—CH, □—DE) and ageing (without (a) and after (b) ageing).

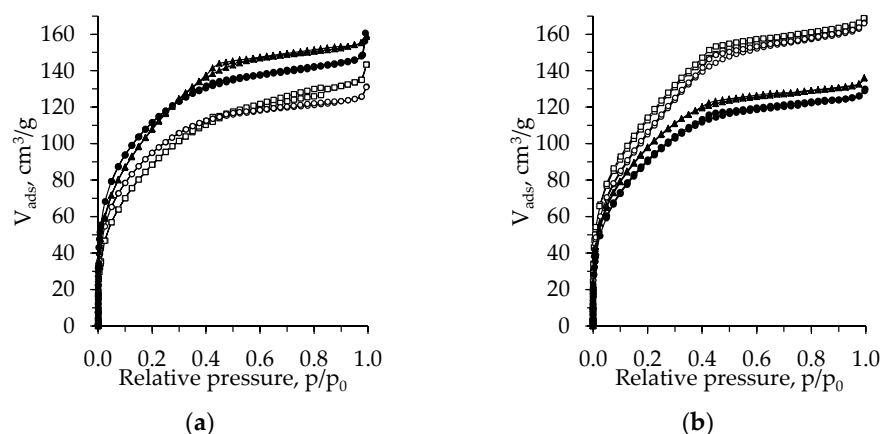


Figure 3. Isotherms of the subcritical dried (800 mbar, 70 °C, 8 h) TiO_2 aerogels (precursor TBOT) versus the type of exchange solvent (●—without exchange, ○—nH, ▲—CH, □—DE) and ageing (without (a) and after (b) ageing).

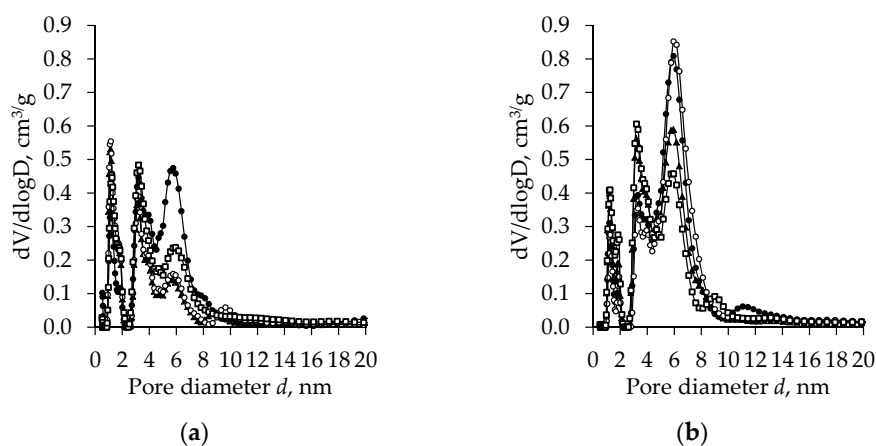


Figure 4. The pore size distribution of the subcritical dried (800 mbar, 70 °C, 8 h) TiO_2 aerogels (precursor TIP) vs. the type of exchange solvent (●—without exchange, ○—nH, ▲—CH, □—DE) and ageing (without (a) and after (b) ageing).

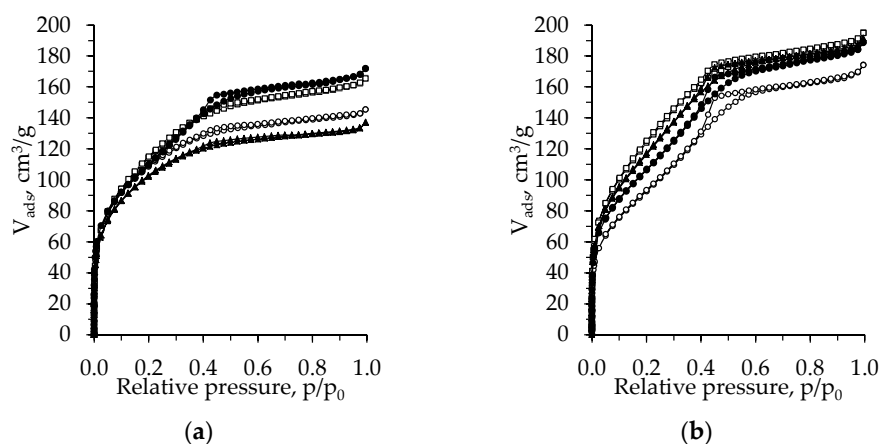


Figure 5. Isotherms of the subcritical dried (800 mbar, 70 °C, 8 h) TiO_2 aerogels (precursor TIP) vs. the type of exchange solvent (●—without exchange, ○—nH, ▲—CH, □—DE) and ageing (without (a) and after (b) ageing).

Figure 2 shows pore size distribution curves of the unaged and aged TiO_2 aerogels obtained using the precursor TBOT and additionally exchanged in different solvents. For the unaged and without an additional exchange-synthesized aerogels, the pore diameter

distribution curve has four peaks. The highest peak was found at 1 and 4.0 nm, twice as low at 6 nm, and the lowest peak was found at 14 nm. The character of the pore size distribution curve changes substantially after the additional solvent exchange. In the case when CH is used, the first three peaks remain in the pore distribution curves with their peaks being in the same position as the samples without an additional exchange, but their height is lower. The heights of the first and second peak are about twice as low and those of the third peak are about 1.4 times lower compared to the samples for which an additional exchange was not applied. The additional solvent exchange with DE and nH results in radical changes in the pore distribution mode. The unimodal pore size distribution indicates a decrease in the polydispersity of the system. The highest probability of the diameter of the pores in these aerogels is 0.5–3 nm, and the number of the larger pores in these aerogels is insignificant.

Aging changes the nature of the pore size distribution curves for these aerogels (Figure 2b). The pore distribution curves have been changed from polymodal to unimodal with a peak in the range from 1 to 4 nm for the aerogels without an additional exchange or additionally CH-exchanged. Compared to the unaged samples without an additional exchange, the peak height after aging was 2-fold decreased, but the width of the peak increased. After the aerogels were aged and additionally exchanged in the solvents nH and DE, a wider pore size distribution was observed and the mode of the curves was changed from unimodal to curves with three clear expressed peaks. In this case, the effect of the solvent is not efficient as the mode of the curves is very similar. Here, an increase in the number of pores with diameters ranging from 2 to 8 nm is observed.

Figure 3 shows the N₂ adsorption–desorption isotherms of the TiO₂ aerogels from the precursor TBOT, dried under subcritical conditions (800 mbar, 70 °C, 8 h).

The isotherms of the unaged aerogels can be classified as type I with an H4 hysteresis loop. The exception is the CH-exchanged sample, the isotherm of which can be attributed to the type IV isotherm with an H2 hysteresis loop (Figure 3a) [32,33]. After aging, the isotherm of the CH-exchanged sample changes to type I isotherms with an H4 hysteresis loop and that of the nH- and DE-exchanged aerogels to type IV isotherms with an H2 hysteresis loop. For the samples without an additional exchange isotherm type, the hysteresis loop remains the same, while the adsorption values decrease (Figure 3b). The data coincide well with those of the pore size distribution curves (Figure 2).

Three characteristic peaks in the zone from 0–8 nm were observed in the pore size distribution curves of the unaged subcritically dried TiO₂ aerogels synthesized from the precursor TIP (Figure 4a). For the first two peaks, there is no significant influence of the solvent type used for the additional exchange. The peak height decreases slightly with the increasing pore diameter. A more pronounced effect of the additional solvent exchange was observed for the third peak. After the additional nH exchange, the height of the third peak at 6 nm decreased more than twice and a small fourth peak at 9 nm occurred.

The curves of the aged and unaged samples show that aging changes the porosity of the TiO₂ aerogels (Figure 4b). After aging, the nature of the distribution curves of the TiO₂ aerogels synthesized from the precursor TIP remains the same (the curves have three peaks), but there are significant differences in their height. The height of the first peak (nanopore diameter was about 1.0 nm) decreases from 0.6 down to 0.4, the height of the second peak remains virtually unchanged, and the third peak height increases to 0.8 at 6.0 nm. The influence of the solvent used for the additional exchange is also evident. For additionally nH-exchanged samples, the amount of pores with a diameter of 6 nm is higher than for the samples without an additional exchange, for which additional exchanges in other solvents have been used. In other cases, the size and amount of the pores were close to those of the unaged specimens.

Figure 5 shows the N₂ adsorption–desorption isotherms of the TiO₂ aerogels obtained using the precursor TIP. The isotherm of the unaged TiO₂ aerogel without an additional solvent change can be classified as type IV isotherms with an H2 hysteresis loop and the remaining samples can be classified as type I isotherms with an H4 hysteresis loop

(Figure 5a). After aging, the isotherms of all obtained aerogels are changed to type IV with an H2 hysteresis loop (Figure 5b) [32,33].

The influence of aging on the TiO₂ aerogel pore size distribution has been found to be highly dependent on the precursor's nature; however, it is difficult to identify a clear effect of the solvent type used for the additional exchange. It is interesting to state that the same tendency was found under subcritical drying conditions when a 400 mbar pressure was applied [29]. A summary of the BET analysis results is provided in Table 1.

Table 1. The morphology of the TiO₂ aerogels versus precursor, solvent type, and ageing duration.

| Precursor | Ageing Duration, h | Solvent | Surface Area *, m ² /g | Pore Volume *, cm ³ /g | C _{BET} Constant * |
|-----------|--------------------|---------|-----------------------------------|-----------------------------------|-----------------------------|
| TIP | 0 | - | 397.257 | 0.244 | 90.156 |
| | | CH | 373.878 | 0.192 | 84.773 |
| | | nH | 398.166 | 0.206 | 82.372 |
| | | DE | 420.178 | 0.235 | 67.304 |
| | 72 | - | 396.665 | 0.269 | 55.687 |
| | | CH | 439.581 | 0.271 | 47.050 |
| nH | | 351.235 | 0.247 | 45.727 | |
| TBOT | 0 | - | 409.955 | 0.212 | 78.273 |
| | | CH | 404.379 | 0.225 | 49.223 |
| | | nH | 348.767 | 0.182 | 68.408 |
| | | DE | 334.882 | 0.196 | 42.937 |
| | 72 | - | 337.288 | 0.183 | 50.619 |
| | | CH | 363.361 | 0.192 | 57.696 |
| nH | | 399.636 | 0.237 | 43.530 | |
| | | DE | 421.080 | 0.240 | 53.418 |

* The difference in the measured values for the same group does not exceed 5%.

2.4. Raman Analysis

Figure 6 shows the Raman spectra of the original prepared unaged and aged TiO₂ aerogels without an additional solvent exchange. The observed peaks in the Raman shift of 400, 515, and 640 cm⁻¹ can be ascribed to the characteristic vibrational modes B_{1g}(1), A_{1g}(2), and E_g(3) for the anatase phase of the TiO₂. Independently of the precursor's nature, the Raman peaks also appear at the Raman shift, exceeding 800 cm⁻¹. The peaks at 1110–1460, 2872, 2916–2936, and 2952–2969 cm⁻¹ can be attributed to the –CH₃ bending vibration mode, –CH₃ stretching mode, –CH₂ asymmetric stretching mode, and the –CH₃ asymmetric stretching mode, respectively [34,35].

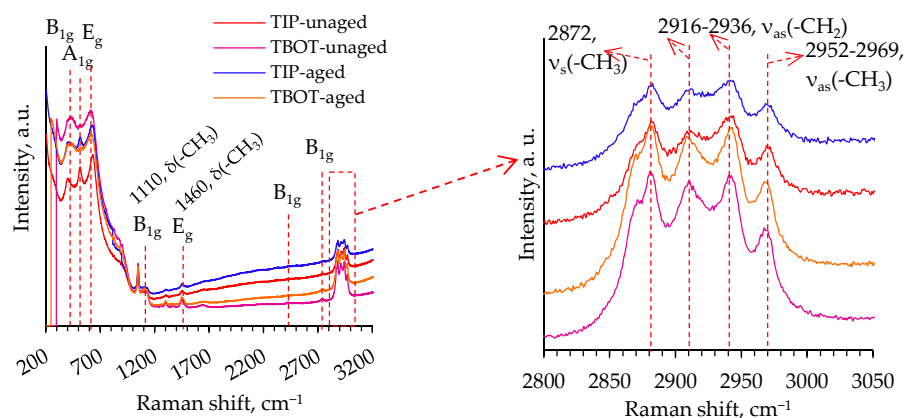


Figure 6. Raman spectra of the unaged and aged TiO₂ aerogels synthesized without an additional solvent exchange.

The results obtained are in a good agreement with the FT-IR and STA results. It is confirmed that after subcritical drying, residues of organic compounds remain in the structure or the pores of the TiO₂ aerogels. The Raman spectra analysis used here shows the formation of the anatase phase in the TiO₂ aerogels.

2.5. Thermal Analysis

In Figure 7, the typical results of the simultaneous thermal analysis (differential thermal (DTA)—Figure 7a,c; thermogravimetric (TG) analysis—Figure 7b,d) of the synthesized aerogels are presented. It is evident that for all DTA curves in the temperature region from 200 °C to 500 °C two peaks are characteristic. The results of these curves are summarized in Tables S1 and 2. The first exothermic peak in Figure 7a,b (Table S1) starts at ~204 °C and continues to ~309 °C and the obtained weight loss (~2.2–6.6%) in this temperature range is probably due to the reaction and the release of residual organic compounds (excluding solvents and alkoxy groups) [36–38]. The second exothermic peak at 368–474 °C can be attributed to the formation of the anatase (Figure 7c,d; Table 2), i.e., the conversion of Ti(OH)₄ into TiO₂ (dehydroxylation) and the occurred crystallization of the anatase [38,39]. The materials do not suffer any thermal changes above 500 °C. A mass loss below ~225 °C in the TG curves can be attributed to adsorbed impurities and moisture [36,39].

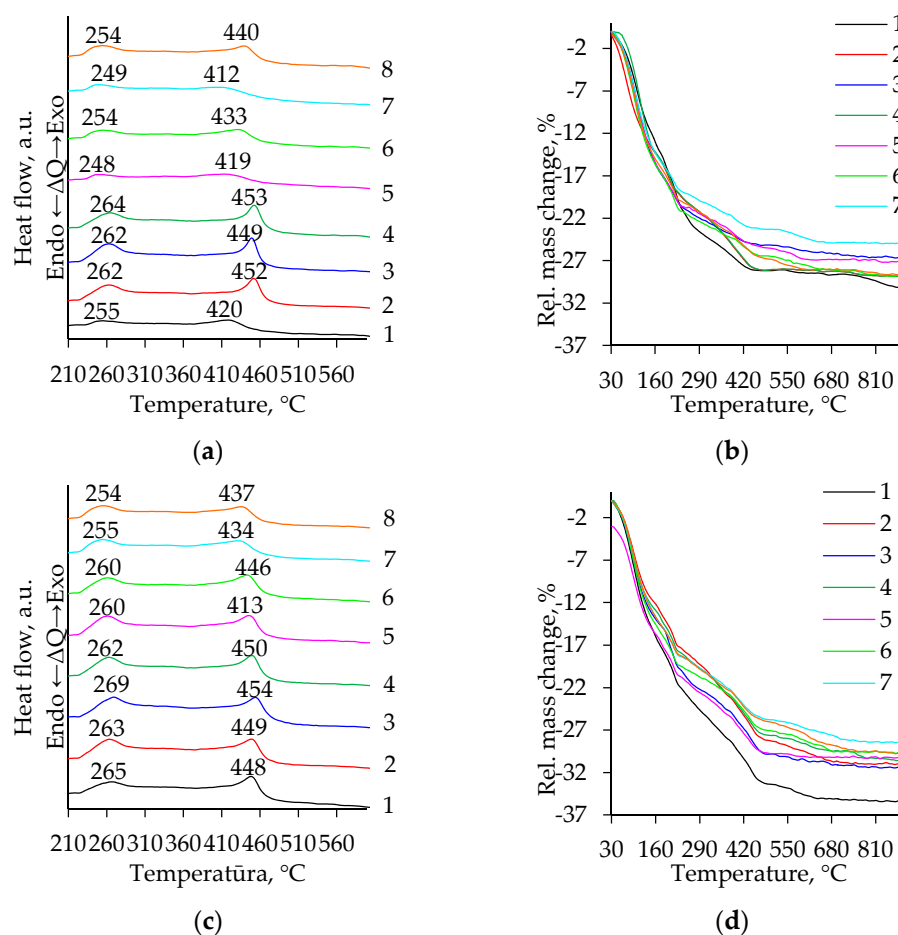


Figure 7. DTA (a,c) and TG (b,d) curves of the TiO₂ aerogels after subcritical drying (800 mbar, 70 °C, 8 h) vs. precursor type (TIP (a,b), TBOT (c,d)), ageing (without ageing (1–4), aged (5–8)), and additional solvent exchanges (1, 5—without exchange; 2, 6—CH; 3, 7—nH; 4, 8—DE).

Table 2. Details of STA curves that are typical for TiO₂ aerogel anatase phase formation.

| Precursor | Ageing Duration, h | Solvent | Peak Characteristics | | | Heat of Process, J/g | Mass Loss, % |
|-----------|--------------------|---------|-------------------------|-----------------------|-----------------------|----------------------|--------------|
| | | | T _{onset} , °C | T _{max} , °C | T _{end} , °C | | |
| TIP | 0 | - | 380.8 | 420.8 | 449.7 | 283.83 | 2.272 |
| | | CH | 428.9 | 452.1 | 467.4 | 678.39 | 3.752 |
| | | nH | 429.2 | 449.4 | 462.7 | 706.00 | 4.279 |
| | | DE | 430.5 | 452.5 | 468.5 | 705.21 | 3.551 |
| | 72 | - | 369.4 | 419.4 | 456.1 | 282.60 | 2.407 |
| | | CH | 388.8 | 432.5 | 458.3 | 385.80 | 2.251 |
| | | nH | 368.9 | 412.4 | 455.2 | 282.95 | 1.863 |
| | | DE | 405.7 | 440.2 | 462.1 | 447.65 | 3.077 |
| TBOT | 0 | - | 418.4 | 448.8 | 465.9 | 651.85 | 5.063 |
| | | CH | 413.1 | 449.4 | 468.0 | 729.47 | 5.118 |
| | | nH | 421.2 | 454.3 | 473.2 | 765.44 | 5.140 |
| | | DE | 418.7 | 450.1 | 466.8 | 714.02 | 4.809 |
| | 72 | - | 410.1 | 446.1 | 464.8 | 703.29 | 4.494 |
| | | CH | 404.3 | 443.8 | 465.1 | 651.50 | 4.175 |
| | | nH | 383.9 | 434.3 | 460.5 | 518.37 | 3.863 |
| | | DE | 392.9 | 437.0 | 460.1 | 446.77 | 3.496 |

The total mass loss was between 25–33% and 27–36% for the samples prepared using the precursors TIP (Figure 7a, Table S1) and TBOT (Figure 7b, Table S1), respectively. For comparison, after the high-temperature supercritical drying, the mass loss in the TG curves is approximately only up to ~5% [40] and this tends to suggest that for supercritical dried samples the decomposition of the organic groups is already reached.

To determine whether the exothermic peak at 368–474 °C in the DTA curves was induced by the formation of the anatase phase, several samples were heat-treated at 500 °C for two hours. This temperature was chosen based on data from the literature [41] and the obtained results (Figure 7, Table 2) are as follows: the anatase phase is formed at a temperature higher than 400 °C. Moreover, the selected calcination temperature must ensure full thermal conversions in the mentioned temperature range. To confirm this, the calcinated samples were investigated by XRD analyses (Figure 8). All calcinated TiO₂ aerogel samples crystallized in the anatase phase (PDF-00-064-0863) [30]. In all investigated cases, the relative intensity of the peaks in the XRD patterns (Figure 8) shows a similar intensity.

For comparison, Table 3 presents the size of the crystallites for aged and unaged TiO₂ aerogels synthesized without a solvent exchange and additionally nH-exchanged. No significant crystallite size was found when the synthesis was performed using the precursor TBOT, while aging resulted in an increase in the crystallite size for the TiO₂ aerogels synthesized from TIP.

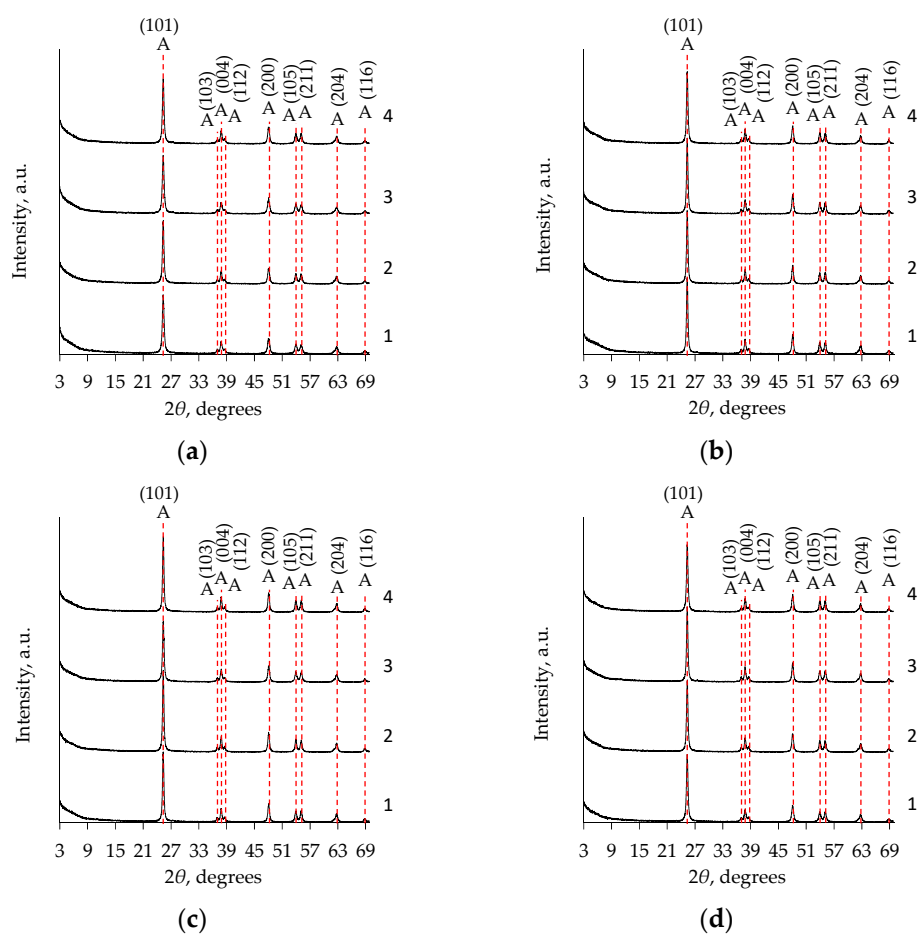


Figure 8. The effects of calcination on the TiO₂ aerogel XRD patterns after subcritical drying (800 mbar, 70 °C, 8 h) in relation to the precursor (TIP (a,b), TBOT (c,d)), ageing (without aging (a,c), aged (b,d)), and additional solvent exchanges (1—without exchange; 2—CH; 3—nH; 4—DE). Indices: A—anatase phase.

Table 3. Variation in crystallite size depending on the TiO₂ aerogel synthesis conditions.

| Precursor | Ageing Duration, h | Solvent | Crystallite Size, nm |
|-----------|--------------------|---------|----------------------|
| TIP | 0 | - | 18.52 |
| | | nH | 18.03 |
| | 72 | - | 20.62 |
| | | nH | 21.60 |
| TBOT | 0 | - | 22.92 |
| | | nH | 20.11 |
| | 72 | - | 20.47 |
| | | nH | 23.08 |

2.6. Morphology of TiO₂ Aerogels

The SEM investigation results show a typical morphology for micrometer-designed aerogel-like powders (Figure 9). Micrometer-sized particles are visible in the samples [12,31,42]. The particles are highly polydispersed and the smallest ones of these are agglomerated. It seems that the particle size tends to decrease after calcination, most probably because of the anatase phase formation.

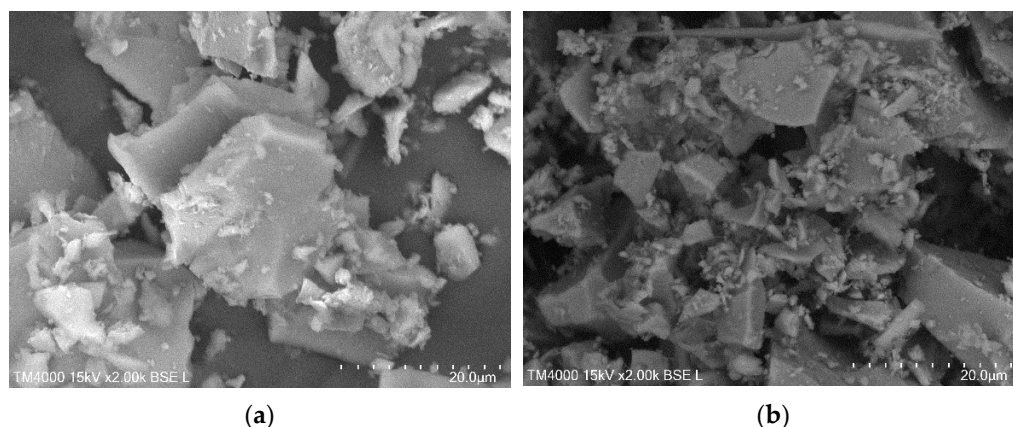


Figure 9. SEM micrographs of aged TiO₂ aerogel (precursor TIP) powders: (a) before calcination; (b) after calcination.

Calcination also results in an increase in both the apparent (ρ_a) and true (ρ_t) density of the aerogels and in a small increase in porosity (Table 4).

Table 4. TiO₂ aerogel density and porosity in relation to the synthesis conditions.

| Precursor | Ageing Duration, h | Solvent | $\rho_a, \text{cm}^3/\text{g}$ | | $\rho_t, \text{cm}^3/\text{g}$ | | Porosity, % | |
|-----------|--------------------|---------|--------------------------------|-------------------|--------------------------------|-------------------|--------------------|-------------------|
| | | | Before Calcination | After Calcination | Before Calcination | After Calcination | Before Calcination | After Calcination |
| TIP | 72 | - | 0.68 | 1.13 | 2.66 | 4.89 | 74 | 77 |
| | | nH | 0.68 | 1.20 | - | - | - | - |
| TBOT | 72 | - | 0.69 | 1.16 | 2.29 | 4.36 | 70 | 73 |
| | | nH | 0.69 | 1.29 | - | - | - | - |

2.7. UV–Vis Spectroscopy Analysis

The optical properties of the synthesized aerogels were evaluated by the UV–vis spectroscopy method. All obtained spectra show a strong UV absorption with a shoulder at about 335–340 nm, which is typical for catalytic titania derivatives (Figure 10a).

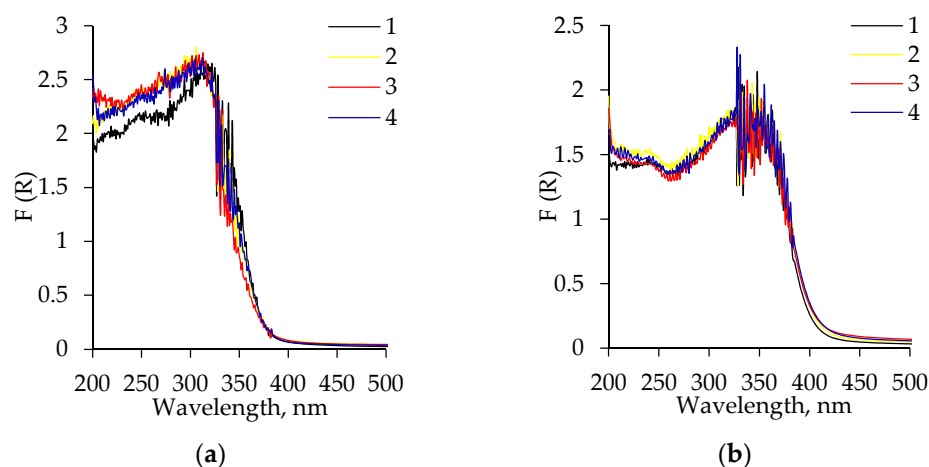


Figure 10. Diffuse reflectance spectra of the aged TiO₂ aerogels: (a) without calcination; (b) after calcination. 1–2 correspond to the precursor TIP and 3–4—to TBOT; 1, 3—without solvent exchange; 2, 4—nH-exchanged.

The calcination leads to a shift in the optical bandgap with 30 nm or longer wavelengths (Figure 10b) [43,44], which are responsible for an increase in the thermal conduc-

tivity (see next section). Surface defects in titania realized by surface diffusion or cationic and anionic doping often lead to a weak coloration or a bandgap shift of ceramic oxide powders [45,46]. The optical bandgap energy E_g of the original and calcinated samples was calculated using the Tauc plot method (Figure 11) [47].

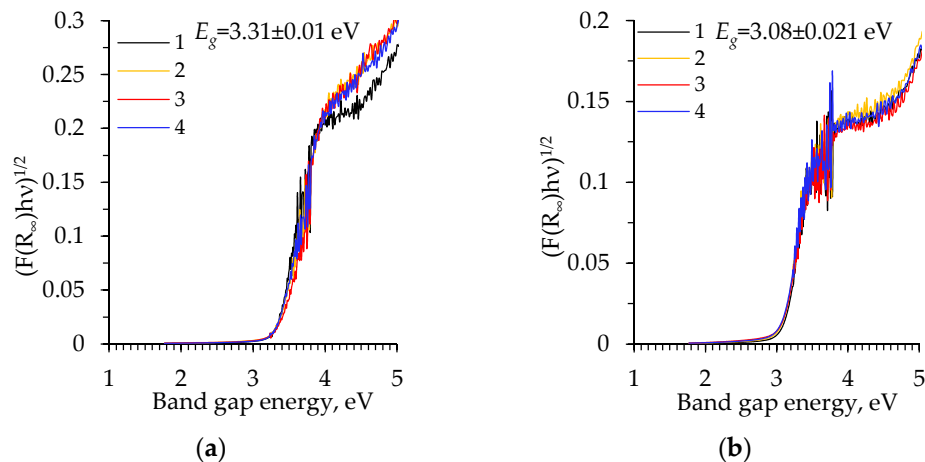


Figure 11. Tauc plot of the aged TiO_2 aerogels: (a) without calcination; (b) after calcination. 1–2 curves correspond to the precursor TIP and 3–4—to TBOT: 1, 3—without solvent exchange; 2, 4—nH-exchanged.

The investigated amorphous TiO_2 aerogels showed a higher indirect bandgap energy ($E_g = 3.31 \pm 0.01$ eV, Figure 11a) compared to the crystalline phase E_g , which is equal to 3.08 ± 0.028 eV (Figure 11b) [48]. The following results are in a good agreement with the data from the literature: the anatase, as an indirect bandgap semiconductor, has a bandgap energy between 3 and 3.2 eV [8,10,44]. These values are very close to those found for the subcritically dried aerogels at a 400 mbar vacuum. [29]. The indirect bandgap energy (E_g) of the uncalcinated samples dried at a 400 mbar vacuum was determined to be equal to 3.32 ± 0.037 eV and for the calcinated samples it was 3.08 ± 0.026 eV. Moreover, the anatase bandgap can be changed by variations in the size of the nanoparticles or the synthesis conditions [11].

2.8. Thermal Conductivity Measurements

The results of the thermal conductivity measurements are presented in Table 5. In the last column of Table 5, the increase in the thermal conductivity of the samples, Δk , as a result of the calcination, is given. An increase in k is detected as a result of the calcination, depending on the initial aerogel chemistry.

Table 5. Results of thermal conductivity measurements of the aged and calcinated TiO_2 aerogel samples.

| Precursor | Solvent | | Thermal Conductivity k^* , W/m·K | Δk After Calcination |
|-----------|---------|-----------------------|---------------------------------------|---------------------------------|
| TIP | nH | Before calcination | 0.085 | - |
| | | | 0.079 | - |
| TBOT | nH | After calcination | 0.084 | - |
| | | | 0.082 | - |
| TIP | nH | After calcination | 0.100 | 0.016 |
| | | | 0.099 | 0.02 |
| TBOT | nH | After calcination | 0.106 | 0.024 |
| | | | 0.105 | 0.023 |

* The relative standard deviation of the measurements (RSD) is 0.7%.

The increase in Δk correlates with the UV–vis measurements, where there is a decrease in the optical bandgap as a result of heating, which is equivalent to an increase in the elec-

trical conductivity. In semiconductors and insulators, the decrease in the optical bandgap is proportional to the electrical conductivity.

The thermal conductivity (k) and electrical conductivity (σ) of the materials are connected by the Wiedemann–Franz law as follows:

$$k/\sigma = LT, \quad (1)$$

where T is the temperature and $L = 2.44 \times 10^{-8} \text{ V}^2\text{K}^{-2}$ [49]. Thus, the increase in the thermal conductivity (Table 3) can be connected with the increase in the electronic contribution to the thermal conductivity.

3. Conclusions

A cost-effective solution for synthesizing high-porosity TiO_2 aerogels, which can be used as mesoporous perovskite network charge-carrier materials during solar cell manufacturing, is developed. The influence of a lower vacuum (800 mbar) and the effect of titanium precursors (TIP and TBOT), solvents (nH, CH, DE) used for an additional solvent exchange, aging, and calcination on the properties of the final products have been investigated. The subcritical dried samples at an 800 mbar vacuum show an amorphous structure, which, after calcination, tends to crystallize in the anatase phase. The size of the crystallites depends on the nature of the precursor. Selected synthesis conditions result in the formation of highly polydispersed aerogels with the highest probability of pore size distribution in the region from 0.5 to 15 nm. The highest diameter of the pores has been found for the additionally nH-exchanged, aged aerogels synthesized from the precursor TIP. Calcination also results in an increase in both the apparent and true density of the aerogels and in an increase in their porosity. Independently of the precursor type, the apparent and true density of the calcinated aerogels increases twice compared to the uncalcinated species. The calcination of the aerogels results in an increase in the thermal conductivity because of an optical bandgap decrease, detected by UV–vis reflectance spectroscopy. The obtained results show that it is meaningful to evaluate the applicability of the synthesized aerogels in perovskite solar cells.

4. Materials and Methods

Titanium (IV) isopropoxide (TIP, 98% Fluorochem, Glossop, UK) and tetrabutyl orthotitanate (TBOT, 95% Fluorochem, Glossop, UK) were used as the titanium sources. Distilled water (H_2O) and ethanol (EtOH, 99.5%, Emparta ASC, Merck-KGaA, Darmstadt, Germany) were used as the solvents. Nitric acid (HNO_3 , 65%, Chempur, Piekary Slaskie, Poland) was used as a catalyst, as well as a chelating agent. Ethanol, n-hexane (nH, 99%, Chempur, Piekary Slaskie, Poland), cyclohexane (CH, 99%, Chempur, Piekary Slaskie, Poland), and diethyl ether (DE, 99.5%, Chempur, Piekary Slaskie, Poland) were used for the solvent exchanges. All the chemical reagents were used as received.

4.1. Synthesis of TiO_2 Aerogels

A TiO_2 aerogel was synthesized through a sol–gel method, earlier reported by our group [29]. Drying of the gel network was performed at a subcritical condition at an 800 mbar vacuum in a vacuum oven at a temperature of 70 °C. The drying duration was 8 h. The main characteristics of the used vacuum system were as follows: chamber (VC50, SalvisLAB, Reussbühl/Lucerne, Switzerland) volume was 50 L and the vacuum system, Vacuubrand PC 8/RC 6 (Vacuubrand GMBH + CO KG, Wertheim, Germany), had a maximum pumping speed of 5.9/6.9 m^3/h . The synthesized samples were sieved through a sieve (with a mesh width of 80 μm). The thermal treatment for part of the samples was carried out at a temperature of 500 °C for a duration of 2 h with a heating rate of 4 °C/min (SNOL 10/1300, SnolTherm business unit, part of Umega Group, AB, Lithuania).

4.2. Characterization

X-ray diffraction (XRD), Fourier-transform infrared spectroscopy (FT-IR), Brunauer–Emmett–Teller (BET), Raman spectroscopy, simultaneous thermal analysis (STA), scanning electron microscopy (SEM), ultraviolet–visible (UV–vis), and thermal conductivity measurements were applied to investigate and compare the properties of the synthesized TiO₂ aerogels and to find out the most effective synthesis route.

Powder X-ray diffraction (XRD) spectra were carried out using a D8 Advance diffractometer (Bruker AXS, Karlsruhe, Germany) (CuK_α radiation was generated at 40 mA and 40 kV, range 2θ = 3–70°, a scanning speed of 6°/min, scan type—a coupled two theta/theta).

For the Fourier-transform infrared (FT-IR) spectroscopy, a Perkin-Elmer FT-IR system spectrometer (Perkin Elmer, Boston, MA, USA) using KBr tablet-shaped samples over the wave-number range from 400 to 4000 cm⁻¹ (±0.01 cm⁻¹) was used.

Brunauer–Emmett–Teller (BET) analysis was performed with the surface area analyzer Autosorb iQ (Quantachrome Instruments, Boynton Beach, FL, USA) using an N₂ gas adsorption isotherm at 77 K.

The bond structure was analyzed by μ-Raman spectroscopy (Renishaw inVia spectrometer, Wotton under Edge, UK) using a 1.5 mW excitation at a wavelength of 532 nm, focused on a 4 μm spot; the exposure duration was 10 s and the accumulation quantity was 5 for the spectral range from 200–3200 cm⁻¹.

An STA (differential scanning calorimetry—DSC and thermogravimetry—TG) using the Linseis instrument STA PT1000 was performed. The heating rate was 15 °C/min and the temperature range was from 30 °C to 950 °C. The test was carried out under air atmosphere using ceramic sample handlers and platinum crucibles.

For SEM, the standard electron microscope Hitachi TM 4000 working on an SE regime was used. The particles were Au-covered.

The apparent density (ρ_a) was calculated by measuring the volume and mass of the aerogels. The porosity was calculated by using the apparent density and true density (ρ_t) as follows:

$$Porosity = \frac{(\rho_t - \rho_a)}{\rho_t} \cdot 100\% \quad (2)$$

The room temperature diffuse reflectance spectra were measured on a Perkin-Elmer (Walham, MA, USA) Lambda 35 spectrophotometer equipped with a reflectance accessory (RSA-PE-20, Labsphere, NorthSutton, NH, USA) and a vertical sample holder with a quartz glass window between 250 nm and 900 nm. As a reference, white and black certified reflectance standards Labsphere[®] were used. The f–f transitions and UV charge transfer transitions (CTT) of Ho₂O₃ and Sm₂O₃ micropowders were used as a reference. The peak maxima and intensities in the region between 250–750 nm were in a good agreement with the theory [50,51]. From the measured diffuse reflectance R (%), the Kubelka–Munk function F(R) was calculated [52].

A Tauc plot method was used to determine the optical energy bandgap (E_g) of the selected samples. The optical absorption strength depends on the difference between the photon energy and the bandgap as follows:

$$(F(R)h\nu)^{1/n} = A(h\nu - E_g) \quad (3)$$

where *h* is the Planck's constant, *ν* is the photon's frequency, *n* = 2 for the indirect allowed transitions, E_g is the bandgap, and *A* is the slope of the Tauc plot in the linear region [47].

The thermal measurements were performed on a C-THERM TCi thermal conductivity analyzer configured with a Modified Plane Source (MTPS) sensor using a TCI small volume test kit (SVTK) for the measurements of powders, foams, and gels.

Supplementary Materials: The following supporting information can be downloaded at: <https://www.mdpi.com/article/10.3390/gels8070422/s1>, Figure S1: XRD patterns of TiO₂ aerogels after subcritical drying (800 mbar, 70 °C, 8 h) without aging (1–4) and after 72 h of aging (5–8) depending on the precursor type (TIP (a), TBOT (b)) and the solvent used for the additional solvent exchange (1, 5—without exchange; 2, 6—CH; 3, 7—nH; 4, 8—DE); Table S1: Details of STA curves that are typical for TiO₂ aerogel organic groups decomposition.

Author Contributions: Conceptualization and writing—original draft preparation, all authors; methodology, J.D. and N.D.; validation, all authors; formal analysis, all authors; investigation, J.D., N.D., S.G. and E.F.-U.; resources, J.D.; writing—review and editing, all authors; visualization, J.D., E.F.-U. and N.D.; supervision, J.D. and J.U.; project administration, J.U.; funding acquisition, J.U. All authors have read and agreed to the published version of the manuscript.

Funding: This research was funded by the European Union Structural Funds (European Regional Development Fund), Instrument: J05-LVPA-K Intellect. Joint business-science projects, grant number J05-LVPA-K-03-0126.

Institutional Review Board Statement: Not applicable.

Informed Consent Statement: Not applicable.

Data Availability Statement: Not applicable.

Acknowledgments: J.D., E.F.-U. and J.U. thank the project “AidaSUN—development of autonomous multifunctional lighting pole with an integrated new generation solar modules system”, No. J05-LVPA-K-03-0126). N.D. and S.G. thank the project CoE “National center of mechatronics and clean technologies” BG05M2OP001-1.001-0008-C01.

Conflicts of Interest: The funders had no role in the design of the study, in the collection, analyses, or interpretation of the data, in the writing of the manuscript, or in the decision to publish the results.

References

1. Yorov, K.E.; Baranchikov, A.E.; Kiskin, M.A.; Sidorov, A.A.; Ivanov, V.K. Functionalization of aerogels with coordination compounds. *Russ. J. Coord. Chem.* **2022**, *48*, 89–117. [[CrossRef](#)]
2. Huang, J.; Wang, X.; Guo, W.; Niu, H.; Song, L.; Hu, Y. Eco-friendly thermally insulating cellulose aerogels with exceptional flame retardancy, mechanical property and thermal stability. *J. Taiwan Inst. Chem. Eng.* **2022**, *131*, 104159. [[CrossRef](#)]
3. Sun, S.; Yan, Q.; Wu, M.; Zhao, X. Carbon aerogel based materials for secondary batteries. *Sustain. Mater. Technol.* **2021**, *30*, e00342. [[CrossRef](#)]
4. Du, L.; Lu, T.; Li, B. CO₂ capture and sequestration in porous media with SiO₂ aerogel nanoparticle-stabilized foams. *Fuel* **2022**, *324*, 124661. [[CrossRef](#)]
5. Wang, X.; Tian, Y.; Yu, C.; Liu, L.; Zhang, Z.; Wu, Y.; Shen, J. Organic/inorganic double-precursor cross-linked alumina aerogel with high specific surface area and high-temperature resistance. *Ceram. Int.* **2022**, *48*, 17261–17269. [[CrossRef](#)]
6. Walker, R.C.; Potochniak, A.E.; Hyer, A.P.; Ferri, J.K. Zirconia aerogels for thermal management: Review of synthesis, processing, and properties information architecture. *Adv. Colloid Interface Sci.* **2021**, *295*, 102464. [[CrossRef](#)]
7. Bernardes, J.C.; Müller, D.; Pinheiro, G.K.; Rambo, C.R. Enhancing the optical transparency of TiO₂ aerogels with high surface area through water-based synthesis. *Opt. Mater.* **2020**, *109*, 110359. [[CrossRef](#)]
8. Ardani, M.; Imani, M.; Tadjarodi, A. Core shell Fe₃O₄@TiO₂/silica aerogel nanocomposite; synthesis and study of structural, magnetic and photocatalytic properties. *Microporous Mesoporous Mater.* **2022**, *338*, 111757. [[CrossRef](#)]
9. Sahare, P.; Alvarez, P.G.; Yanez, J.M.S.; Luna-Bárceñas, G.; Chakraborty, S.; Paul, S.; Estevez, M.; Beilstein, J. Engineered titania nanomaterials in advanced clinical applications. *Beilstein J. Nanotechnol.* **2022**, *13*, 201–218. [[CrossRef](#)]
10. Trinh, T.T.P.N.X.; Giang, N.T.H.; Huong, L.M.; Thinh, D.B.; Dat, N.M.; Trinh, D.N.; Hai, N.D.; Oanh, D.T.Y.; Nam, H.M.; Phong, M.T.; et al. Hydrothermal synthesis of titanium dioxide/graphene aerogel for photodegradation of methylene blue in aqueous solution. *J. Sci. Adv. Mater. Devices* **2022**, *7*, 100433. [[CrossRef](#)]
11. Salehi Taleghani, M.; Salman Tabrizi, N.; Sangpour, P. Enhanced visible-light photocatalytic activity of titanium dioxide doped CNT-C aerogel. *Chem. Eng. Res. Des.* **2022**, *179*, 162–174. [[CrossRef](#)]
12. Giang, N.T.H.; Huy, L.G.; Khoi, V.H.; Phong, H.H.T.; Hai, N.D.; Tai, L.T.; Dat, N.M.; Trinh, D.N.; Phong, M.T.; Hieu, N.H. Enhanced photocatalytic activity of titanium dioxide-doped graphene aerogel towards p-nitrophenol removal from aqueous solutions. *Mater. Technol.* **2022**, 1–12. [[CrossRef](#)]
13. Alwin, S.; Sahaya Shajan, X.; Ranjini, M.; Nabhiraj, P.Y.; Ananthapadmanabhan, P.V. Plasma treated TiO₂ aerogel nanostructures as photoanode material and its influence on the performance of quasi-solid dye-sensitized solar cells. *Mater. Res. Bull.* **2017**, *86*, 201–208. [[CrossRef](#)]

14. Liang, S.; Wang, X.; Cheng, Y.-J.; Xia, Y.; Müller-Buschbaum, P. Anatase titanium dioxide as rechargeable ion battery electrode—A chronological review. *Energy Stor. Mater.* **2022**, *45*, 201–264. [[CrossRef](#)]
15. Macwan, D.P.; Dave, P.N.; Chaturvedi, S. A review on nano-TiO₂ sol–gel type syntheses and its applications. *J. Mat. Sci.* **2011**, *46*, 3669–3686. [[CrossRef](#)]
16. Aboulouard, A.; Gultekin, B.; Can, M.; Erol, M.; Jouaiti, A.; Elhadadi, B.; Zafer, C.; Demic, S. Dye sensitized solar cells based on titanium dioxide nanoparticles synthesized by flame spray pyrolysis and hydrothermal sol-gel methods: A comparative study on photovoltaic performances. *J. Mater. Res. Technol.* **2020**, *9*, 1569–1577. [[CrossRef](#)]
17. Ramesh, S.C.; Ramkumar, P.; Columbus, C.C.; Shajan, X.S. Experimental and simulation studies of platinum-free counter electrode material for titania aerogel-based quasi-solid dye-sensitized solar cell. *IEEE J. Photovolt.* **2020**, *10*, 1757–1761. [[CrossRef](#)]
18. Pinheiro, G.K.; Serpa, R.B.; de Souza, L.V.; Sartorelli, M.L.; Reis, F.T.; Rambo, C.R. Increasing incident photon to current efficiency of perovskite solar cells through TiO₂ aerogel-based nanostructured layers. *Colloids Surf. A Physicochem. Eng. Asp.* **2017**, *527*, 89–94. [[CrossRef](#)]
19. Aitola, K.; Gava Sonai, G.; Markkanen, M.; Jaqueline Kaschuk, J.; Hou, X.; Miettunen, K.; Lund, P.D. Encapsulation of commercial and emerging solar cells with focus on perovskite solar cells. *Sol. Energy* **2022**, *237*, 264–283. [[CrossRef](#)]
20. Moussaoui, R.; Elghniji, K.; ben Mosbah, M.; Elaloui, E.; Moussaoui, Y. Sol–gel synthesis of highly TiO₂ aerogel photocatalyst via high temperature supercritical drying. *J. Saudi Chem. Soc.* **2017**, *21*, 751–760. [[CrossRef](#)]
21. Zu, G.; Shen, J.; Wang, W.; Lian, Y.; Zou, L.; Zhang, Y.; Liu, B.; Zhang, F. Heat-resistant, strong titania aerogels achieved by supercritical deposition. *J. Supercrit. Fluids* **2015**, *106*, 145–151. [[CrossRef](#)]
22. Yue, X.; Xiang, J.; Chen, J.; Li, H.; Qiu, Y.; Yu, X. High surface area, high catalytic activity titanium dioxide aerogels prepared by solvothermal crystallization. *J. Mater. Sci. Technol.* **2020**, *47*, 223–230. [[CrossRef](#)]
23. Kim, Y.N.; Shao, G.N.; Jeon, S.J.; Imran, S.M.; Sarawade, P.B.; Kim, H.T. Sol–gel synthesis of sodium silicate and titanium oxychloride based TiO₂–SiO₂ aerogels and their photocatalytic property under UV irradiation. *Chem. Eng. J.* **2013**, *231*, 502–511. [[CrossRef](#)]
24. Alwin, S.; Ramasubbu, V.; Shajan, X.S. TiO₂ aerogel–metal organic framework nanocomposite: A new class of photoanode material for dye-sensitized solar cell applications. *Bull. Mater. Sci.* **2018**, *41*, 27. [[CrossRef](#)]
25. Dutoit, D.C.M.; Schneider, M.; Hutter, R.; Baiker, A. Titania–silica mixed oxides: IV. Influence of Ti content and aging on structural and catalytic properties of aerogels. *J. Catal.* **1996**, *161*, 651–658. [[CrossRef](#)]
26. Kitazawa, N.; Watanabe, Y. Preparation of mesoporous oxide films via block copolymer templating. *J. Non-Cryst. Solids* **2010**, *356*, 109–113. [[CrossRef](#)]
27. Ganesamoorthy, R.; Vadivel, V.K.; Kumar, R.; Kushwaha, O.S.; Mamane, H. Aerogels for water treatment: A review. *J. Clean. Prod.* **2021**, *329*, 129713. [[CrossRef](#)]
28. Chen, Y.X.; Hendrix, Y.; Schollbach, K.; Brouwers, H.J.H. A silica aerogel synthesized from olivine and its application as a photocatalytic support. *Constr. Build. Mater.* **2020**, *248*, 118709. [[CrossRef](#)]
29. Doneliene, J.; Fataraitė-Urbonienė, E.; Rudzikas, M.; Pakalka, S.; Dančhova, N.; Ulbikas, J. Effect of precursor nature and sol-gel synthesis conditions on TiO₂ aerogel's structure. *Molecules* **2021**, *26*, 5090. [[CrossRef](#)]
30. Sui, R.; Rizkalla, A.; Charpentier, P.A. Experimental study on the morphology and porosity of TiO₂ aerogels synthesized in supercritical carbon dioxide. *Microporous Mesoporous Mater.* **2011**, *142*, 688–695. [[CrossRef](#)]
31. Viet, T.Q.Q.; Khoi, V.H.; Thi Huong Giang, N.; Thi Van Anh, H.; Dat, N.M.; Phong, M.T.; Hieu, N.H. Statistical screening and optimization of photocatalytic degradation of methylene blue by ZnO–TiO₂/rGO nanocomposite. *Colloids Surf. A Physicochem. Eng. Asp.* **2021**, *629*, 127464. [[CrossRef](#)]
32. Lowell, S.; Shields, J.E.; Thomas, M.A.; Thommes, M. *Characterization of Porous Solids and Powders: Surface Area, Pore Size and Density*; Particle Technology Series; Springer: New York, NY, USA, 2004; Volume 16, pp. 11–14, 43–45. [[CrossRef](#)]
33. Nawaz, M.; Miran, W.; Jang, J.; Lee, D.S. One-step hydrothermal synthesis of porous 3D reduced graphene oxide/TiO₂ aerogel for carbamazepine photodegradation in aqueous solution. *Appl. Catal. B Environ.* **2017**, *203*, 85–95. [[CrossRef](#)]
34. Wei, X.; Cai, H.; Feng, Q.; Liu, Z.; Ma, D.; Chen, K.; Huang, Y. Synthesis of co-existing phases Sn–TiO₂ aerogel by ultrasonic-assisted sol-gel method without calcination. *Mater. Lett.* **2018**, *228*, 379–383. [[CrossRef](#)]
35. Parale, V.G.; Kim, T.; Phadtare, V.D.; Yadav, H.M.; Park, H.-H. Enhanced photocatalytic activity of a mesoporous TiO₂ aerogel decorated onto three-dimensional carbon foam. *J. Mol. Liq.* **2019**, *277*, 424–433. [[CrossRef](#)]
36. Borrás, A.; Gonçalves, G.; Marbán, G.; Sandoval, S.; Pinto, S.; Marques, P.A.A.P.; Fraile, J.; Tobias, G.; López-Periago, A.M.; Domingo, C. Preparation and characterization of graphene oxide aerogels: Exploring the limits of supercritical CO₂ fabrication methods. *Chem. Eur. J.* **2018**, *24*, 15903–15911. [[CrossRef](#)]
37. Durães, L.; Ochoa, M.; Rocha, N.; Patrício, R.; Duarte, N.; Redondo, V.; Portugal, A. Effect of the drying conditions on the microstructure of silica based xerogels and aerogels. *J. Nanosci. Nanotechnol.* **2012**, *12*, 6828–6834. [[CrossRef](#)]
38. Habibi, S.; Jamshidi, M. Synthesis of TiO₂ nanoparticles coated on cellulose nanofibers with different morphologies: Effect of the template and sol-gel parameters. *Mater. Sci. Semicond. Process.* **2020**, *109*, 104927. [[CrossRef](#)]
39. Cesnovar, A.; Paunovic, P.; Grozdanov, A.; Makreski, P.; Fidanchevska, E. Preparation of nano-crystalline TiO₂ by sol-gel method using titanium tetraisopropoxide (TTIP). *Adv. Nat. Sci. Theory Appl.* **2012**, *1*, 133–142. Available online: https://www.researchgate.net/publication/234164554_Preparation_of_nano-crystalline_TiO2_by_sol-gel_method_using_titanium_tetraisopropoxide_TTIP (accessed on 7 June 2022).

40. Kong, Y.; Shen, X.-D.; Cui, S. Direct synthesis of anatase TiO₂ aerogel resistant to high temperature under supercritical ethanol. *Mater. Lett.* **2014**, *117*, 192–194. [[CrossRef](#)]
41. Poo-arporn, Y.; Luengprasert, K.; Tonlublaio, S.; Loiha, S.; Ruangvittayanon, A.; Poo-arporn, R.P. The influence of calcination temperature on (photo)electrochemical property of TiO₂ prepared by the sol-gel method. *IOP Conf. Ser. Mater. Sci. Eng.* **2020**, *965*, 012005. [[CrossRef](#)]
42. Nateq, M.H.; Ceccato, R. Sol-gel synthesis of TiO₂ nanocrystalline particles with enhanced surface area through the reverse micelle approach. *Adv. Mater. Sci. Eng.* **2019**, *2019*, 1567824. [[CrossRef](#)]
43. Gonçalves, M.C.; Pereira, J.C.; Matos, J.C.; Vasconcelos, H.C. Photonic band gap and bactericide performance of amorphous sol-gel titania: An alternative to crystalline TiO₂. *Molecules* **2018**, *23*, 1677. [[CrossRef](#)] [[PubMed](#)]
44. Luna, A.L.; Matter, F.; Schreck, M.; Wohlwend, J.; Tervoort, E.; Colbeau-Justin, C.; Niederberger, M. Monolithic metal-containing TiO₂ aerogels assembled from crystalline pre-formed nanoparticles as efficient photocatalysts for H₂ generation. *Appl. Catal. B Environ.* **2020**, *267*, 118660. [[CrossRef](#)]
45. Gutzov, S.; Lerch, M. Preparation and optical properties of Zr-Ce-O-N materials. *J. Europ. Ceram. Soc.* **2001**, *21*, 595–601. [[CrossRef](#)]
46. Tsekov, R.; Evstatieva, E.; Smirniotis, P.G. Surface diffusion control of the photocatalytic oxidation in air/TiO₂ heterogeneous reactors. *Phys. Chem. Comm.* **2002**, *5*, 161–164. [[CrossRef](#)]
47. Kim, Y.N.; Hwang, H.M.; Wang, L.; Kim, I.; Yoon, Y.; Lee, H. Solar-light photocatalytic disinfection using crystalline/amorphous low energy bandgap reduced TiO₂. *Sci. Rep.* **2016**, *6*, 25212. [[CrossRef](#)] [[PubMed](#)]
48. Saha, D.; Ajimsha, R.S.; Rajiv, K.; Mukherjee, C.; Gupta, M.; Misra, P.; Kukreja, L.M. Spectroscopic ellipsometry characterization of amorphous and crystalline TiO₂ thin films grown by atomic layer deposition at different temperatures. *Appl. Surf. Sci.* **2014**, *315*, 116–123. [[CrossRef](#)]
49. Johnes, W.; March, N.H. *Theoretical Solid State Physics*; Courier Dover Publications: New York, NY, USA, 1985.
50. Petrov, V.; Danchova, N.; Gutzov, S. Temperature dependent optical spectroscopy: A study of holmium diphenanthroline nitrate in DMF. *Spectrochim. Acta Part A Mol. Biomol. Spectrosc.* **2020**, *227*, 117527. [[CrossRef](#)]
51. Gutzov, S.; Ahmed, G.; Petkova, N.; Füglein, E.; Petkov, I. Preparation and optical properties of samarium doped sol-gel materials. *J. Non-Cryst. Solids* **2008**, *354*, 3438–3442. [[CrossRef](#)]
52. Schmidt, W. *Optische Spektroskopie*; Wiley-VCH: Weinheim, Germany, 2000; pp. 273–307.